



Cite this: *Nanoscale*, 2015, 7, 12878

Evolution of magnetism on a curved nano-surface

D. G. Merkel,^{*a,d} D. Bessas,^a Z. Zolnai,^b R. Ruffer,^a A. I. Chumakov,^a H. Paddubrouskaya,^c C. Van Haesendonck,^c N. Nagy,^b A. L. Tóth^b and A. Deák^b

To design custom magnetic nanostructures, it is indispensable to acquire precise knowledge about the systems in the nanoscale range where the magnetism forms. In this paper we present the effect of a curved surface on the evolution of magnetism in ultrathin iron films. Nominally 70 Å thick iron films were deposited in 9 steps on 3 different types of templates: (a) a monolayer of silica spheres with 25 nm diameter, (b) a monolayer of silica spheres with 400 nm diameter and (c) for comparison a flat silicon substrate. *In situ* iron evaporation took place in an ultrahigh vacuum chamber using the molecular beam epitaxy technique. After the evaporation steps, time differential nuclear forward scattering spectra, grazing incidence small angle X-ray scattering images and X-ray reflectivity curves were recorded. In order to reconstruct and visualize the magnetic moment configuration in the iron cap formed on top of the silica spheres, micromagnetic simulations were performed for all iron thicknesses. We found a great influence of the template topography on the onset of magnetism and on the developed magnetic nanostructure. We observed an individual magnetic behaviour for the 400 nm spheres which was modelled by vortex formation and a collective magnetic structure for the 25 nm spheres where magnetic domains spread over several particles. Depth selective nuclear forward scattering measurements showed that the formation of magnetism begins at the top region of the 400 nm spheres in contrast to the 25 nm particles where the magnetism first appears in the region where the spheres are in contact with each other.

Received 5th May 2015,
Accepted 22nd June 2015
DOI: 10.1039/c5nr02928g

www.rsc.org/nanoscale

1. Introduction

The immense spread of internet and cloud computing requires a constant development of data storage devices. Nowadays, discoveries such as giant magnetoresistance (GMR),^{1,2} tunneling magnetoresistance (TMR)^{3,4} and innovations like dynamic flying height (DFH)⁵ or perpendicular magnetic recording (PMR)^{6–8} made possible the continuous increase of stored information on a unit surface area. However, exceeding 1 Tbit per inch² storage density is not possible with the latter techniques⁹ and hence further developments are essential. The next generation of high density recording technologies such as thermally assisted recording (TAR)^{10,11} combined with bit patterned media (BPM)^{12,13} extends the theoretical storage limit as high as 20 Tbit per inch².¹⁴ In order to develop efficient BPM devices, there is a strong demand for nanosystems with an ordered structure. Several methods like electrodeposition,¹⁵ etching,¹⁶ self-assembly,^{17–21} electron-beam lithography^{22,23}

and others^{24–26} are known for producing highly ordered nanostructures. Self-assembled spherical nanoparticles prepared by the Langmuir–Blodgett technique^{27,28} are great candidates for future BPM devices due to their cost effective and large scale preparation. Because of the curved surface, magnetic thin films on such a spherical template exhibit unusual properties. Several theoretical and experimental studies have been reported discussing this phenomenon. It has been shown that a Co/Pd multilayer on the top of self-assembled spherical particles can exhibit radially symmetric anisotropy orientation.²⁹ On the same system, serpentine-like magnetic domain patterns were observed reflecting the topographic structure.³⁰ Chirality frustrated vortex states were found in soft magnetic Permalloy caps induced by the reduced coupling between particles.³¹ Anisotropic magnetostatic interactions were evidenced in the case of rolled nanomembranes induced by a thickness gradient³² and also several magnetic simulations were done to study magnetism in curved surfaces.³³

To have a better understanding of such systems it is indispensable to investigate magnetic thin films in the thickness range where magnetism starts to evolve. To avoid external effects *in situ* experiments are needed, which have been great challenges due to the dedicated sample environment. Such experiments have been performed by K. Schlage and co-workers where the formation of magnetism in iron on highly ordered vertical cylindrical templates was studied.³⁴

^aEuropean Synchrotron Radiation Facility, F-38043 Grenoble, France.

E-mail: dmerkel@esrf.fr

^bCentre for Energy Research, Institute of Technical Physics and Materials Science, P.O.B. 49, H-1525 Budapest, Hungary

^cKU Leuven, Solid-State Physics and Magnetism Section, BE-3001 Leuven, Belgium

^dInstitute for Particle and Nuclear Physics, Wigner Research Centre for Physics, Hungarian Academy of Sciences, H-1525 Budapest, P.O. Box 49, Hungary

In this work, comprehensive characterization using the combination of *in situ* and *ex situ* tools, *i.e.* time resolved grazing incidence nuclear forward scattering (NFS), grazing incidence small angle X-ray scattering (GISAXS), X-ray reflectometry (XRR), atomic and magnetic force microscopy (AFM, MFM), field emission scanning electron microscopy (FESEM), and various calculation methods – vertical susceptibility profiles, micromagnetic simulations – has been applied to understand the onset and evolution of magnetism appearing on the top of spherical templates. Our study can help in exploring the potential and the limits of the formation of magnetic nanostructures in the applied size range of the nanoparticles, interparticle distances and magnetic layer thicknesses.

2. Experimental and methods

Single monolayers of silica spheres with nominal diameters of 25 nm and 400 nm were prepared on top of silicon wafers using the Langmuir–Blodgett technique with controlled hydrolysis of tetraethyl orthosilicate (Stöber's method³⁵). The nanosphere-film deposition was carried out in the Centre for Energy Research, Institute of Technical Physics and Materials Science in Budapest by using a KSV2000 film balance using the vertical deposition method. The (100)Si substrates were cleaned with a 2% HF solution, rinsed with de-ionized (Milli-Q) water and dried at room temperature. The sol samples were homogenized for 10 min in an ultrasonic bath and spread onto the water surface in the film balance. After evaporation of the spreading liquid the layer was compressed at a rate of 40 cm² min⁻¹. The surface-pressure of the layer was monitored by the Wilhelmy-plate method. At *ca.* 80% of the collapse pressure, the surface-pressure of the sample was kept constant for 15 min. Afterwards the monolayer was deposited on the substrate with a withdrawal speed of 5 mm min⁻¹. The films were dried at ambient temperature.

The Langmuir–Blodgett monolayers were analyzed by Field Emission Scanning Electron Microscopy (FESEM) using a LEO 1540 XB Cross-Beam system. The size distribution analysis of the nanospheres resulted in 26 nm and 398 nm median diameters with a Full Width at Half Maximum (FWHM) of 11 nm and 54 nm, respectively (Fig. 1). In the case of the 400 nm particles, the mean interparticle distance was found to be 63 nm with an FWHM of 50 nm. The local hexagonal symmetry of the spheres vanishes on a long scale and the hexagonal cells start to arrange in a twisted pattern.^{36,37} This feature is a consequence of the size distribution of the silica spheres and the domain-like structure of the deposited monolayer. The 25 nm particle template consists of closely packed domains and a smaller amount of particle free regions. Since the closely packed domains give ~90% of the full coverage, we consider an interparticle distance of 0 nm indicating that the particles are in direct contact.

Nominally a 70 Å thick ⁵⁷Fe layer was evaporated in 9 steps, on top of the nanospheres as well as on a flat silicon substrate. The deposition was carried out using the molecular beam

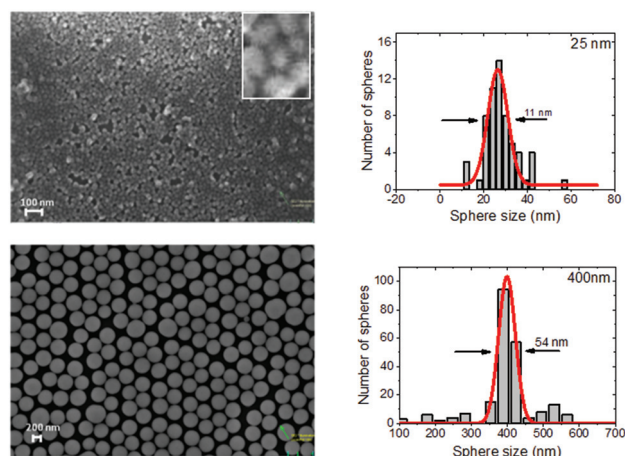


Fig. 1 FESEM image of 25 nm (top) and 400 nm (bottom) diameter silica spheres deposited on the silicon substrate (left) with the results of size distribution analysis (right).

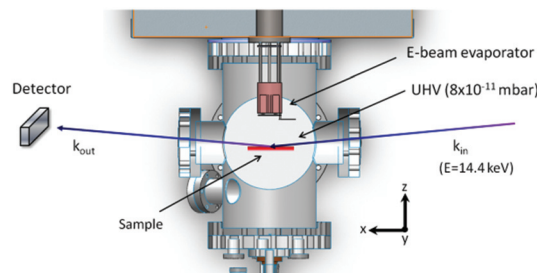


Fig. 2 The arrangement of the *in situ* experiment. The sample situated in a UHV chamber where the electron-beam evaporator was mounted and the synchrotron radiation enters and exits through beryllium windows.

epitaxy (MBE) technique in a UHV³⁸ system at the Nuclear Resonance Beamline ID18³⁹ at European Synchrotron Radiation Facility (ESRF). Prior to deposition, the wafers were annealed at 500 °C for 30 minutes in order to remove any surface contamination. ⁵⁷Fe was evaporated from a rod using an Oxford Applied Research 4-pocket electron-beam evaporator which was mounted on the nuclear resonant scattering (NRS) chamber³⁸ of the UHV system (Fig. 2). The base pressure was 8 × 10⁻¹¹ mbar and increased to 1 × 10⁻¹⁰ mbar during evaporation. After each deposition step, *in situ* time differential grazing incidence nuclear forward scattering (from this point, nuclear forward scattering, NFS) spectra and X-ray reflectivity (XRR) curves were recorded using a 32 element avalanche photodiode detector system with a sub-nanosecond time resolution and grazing incidence small angle X-ray scattering (GISAXS) images were acquired utilizing a standard ESRF MAXIPIX2⁴⁰ image plate. The experiment was performed at 14.412 keV, the excitation energy of the ⁵⁷Fe nucleus, using a high resolution monochromator with 2 meV energy resolution.

After the synchrotron radiation experiment the sample was covered with 5 nm niobium to avoid surface oxidation. The magnetic structure, together with the surface topography were studied using atomic force microscopy (AFM) and magnetic force microscopy (MFM) at KU Leuven. The magnetization measurements were carried out with a Dimension 3100 scanning probe microscope (Bruker Inc.) operated in the tapping/lift mode using commercial MFM probes with tips magnetized along the tip axis. The MFM measurements presented in this article are performed in a lift mode of operation, *i.e.* using a dual pass technique for each scan line and the frequency of the cantilever was near its resonant frequency (~ 60 kHz). During the first pass the AFM topography data are recorded. Then the tip is raised (typically 20–50 nm) and a second scan is performed while maintaining a constant separation between the tip and the local surface topography. This second MFM scan is sensitive to the out-of-plane magnetization. Comparing the MFM image with the corresponding AFM image allows us to establish correlations between the domain structure and the topographic data.

The AFM, MFM and FESEM images were evaluated using Gwyddion⁴¹ and WSxM⁴² software.

The magnetic moment configuration was studied by micro-magnetic simulations. We used NMAG,⁴³ which is an open source, python based software, in order to perform the finite element calculations based on the Landau-Lifshitz and Gilbert equation.⁴⁴ The obtained simulations were visualized using ParaView,⁴⁵ an open-source, multi-platform data analysis and visualization application.

The evaluation of the XRR data was done by using the program FitSuite,⁴⁶ which calculates the reflectivity based on differential propagation matrices.⁴⁷

The GISAXS simulations were done by using BornAgain,⁴⁸ an open source, multiplatform software package which utilizes Distorted Wave Born Approximation (DWBA) in the physical description of the scattering process.

3. Results and discussion

In order to study the evolution of magnetism in the deposited iron layer, first the growth mechanism should be investigated. The XRR curves were recorded after each deposition step on the 25 nm and 400 nm diameter silica nanospheres and on the flat silicon substrate (Fig. 3c–e). The red lines correspond to the fits of the data (black circles) and the numbers indicate the determined iron thicknesses after each evaporation step.

In our model the monolayer of nanospheres was divided into ten sublayers and an average susceptibility χ was assigned to each of the sublayers (Fig. 3a). The susceptibility can be expressed as $\chi = (4\pi N/k^2)f$ and is related to the refractive index as $n = I + \chi/2$.⁴⁹ Here N is the density of the scattering centers, k is the vacuum wavenumber, I is the unit matrix and f is the scattering amplitude.

The three main features in the reflectivity curve: the critical angle, the frequency of oscillations and the slope of the decay carry information about the refractive index (or susceptibility) of the material and the thickness as well as the surface roughness of the layer (Fig. 3b). The critical angle of a X-ray reflectivity curve is $\theta_c = \sqrt{2\delta}$, where δ is proportional to the electron density of the material. In the case of the pristine templates, a well defined critical angle at about 0.13 degrees can be seen. With increasing iron thickness, the most intense change in the total reflection region appears in the case of the flat sample (Fig. 3c). Since the evaporated iron forms a homogeneous layer on the substrate the shift of the critical angle becomes more and more pronounced. However, if the amplitude of the Kiessig oscillation has an extreme at the vicinity of the critical angle, it alters the continuity of this shift which is evidenced at higher iron thicknesses by the shift of the critical angle to higher angles. In the case of 400 nm diameter spheres (Fig. 3e), hardly any change of the critical angle can be seen, only the Kiessig oscillations appear evidencing iron evaporation. The reason for this is that the iron layer cannot form a

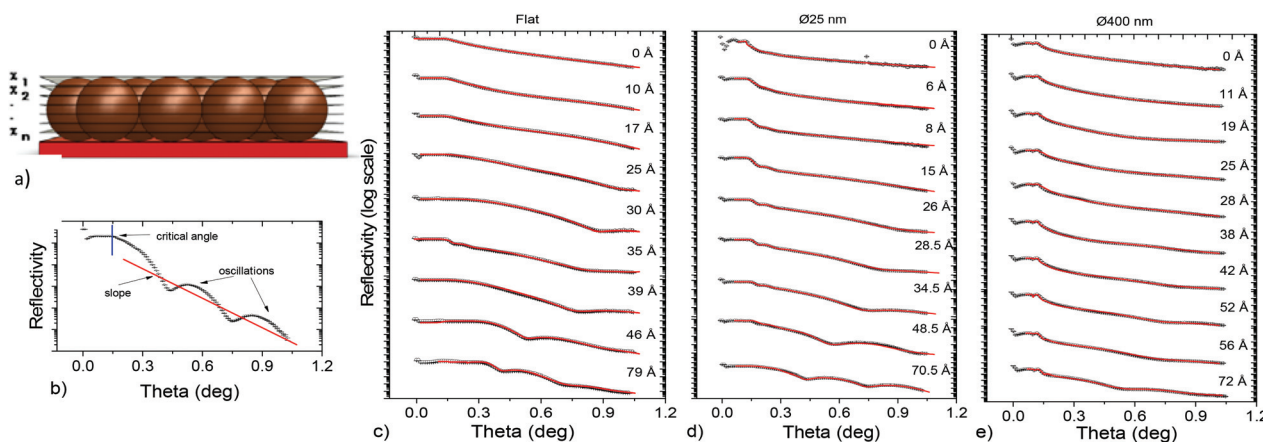


Fig. 3 (a) Division of the spherical particle template into sublayers; (b) a selected reflectivity curve and the definition of the key features such as critical angle, oscillations and the slope of the decay are marked. X-ray reflectivity curves of increasing iron layer thickness on a flat silicon substrate (c) and on 25 nm (d) and 400 nm (e) diameter silica spheres (black points). The red lines correspond to the fits of the data.

laterally homogeneous layer due to the topography and hence the average density of a sublayer never overcomes the density of the silicon substrate. The change of the X-ray reflectivity curve of the 25 nm diameter sphere sample (Fig. 3d) is between the two previously discussed templates. At very low iron thicknesses the reflectivity curve behaves similarly to the 400 nm samples. After 8 Å thick evaporated iron, a small plateau corresponding to the iron critical angle appears and with further iron evaporation becomes more and more dominant.

The frequency of the Kiessig oscillation is a function of layer thickness and the refractive index. This oscillation above the critical angle is superposed to an $\sim 1/\theta^4$ decay, where θ is the incident angle. The decrease of the reflected intensity can be further changed by the surface roughness, according to $e^{-k_z^i k_z^r \sigma^2}$ expression, where σ is the uncorrelated surface roughness and k_z^i , k_z^r are the vertical components of the incident and refracted wave number of the beam. The surface roughness of the flat sample was 9 Å while the iron layer started with the roughness of 5 Å and increased to 10 Å for the thickest layer. For the spherical templates it is more difficult to define roughness. From one hand side there is a substrate roughness which is 10 Å for both sizes but also a roughness between the sublayers were defined in order to smooth out the susceptibility profile. Finally the upper most layer has a separate roughness which was between 2 Å and 6 Å for the 400 nm diameter and between 1 Å and 7 Å for the 25 nm diameter samples.

In order to reconstruct the nanosphere structure as well as the vertical distribution (z direction) of the iron layer on top of the nanospheres the sublayer susceptibilities were determined by analyzing the reflectivity curves. In Fig. 4 the variation of the susceptibility as a function of the position along z axis is presented for the 25 nm diameter (a) and 400 nm diameter (b) silica spheres. All susceptibility curves have a constant value in the “negative” region along the z axis representing the silicon substrate. At zero position (surface of the substrate) where no iron was deposited, the susceptibility profile drops and then follows the curvature of the spheres as their cross section in the sublayer varies with the thickness along the z -axis.

As expected, the shape of the profiles is similar for the two sphere sizes. However, when the iron layer is evaporated, the shape of the profiles changes differently. In the case of the 25 nm diameter spheres the evaporated iron thickness is comparable to the sphere size resulting in a significant change in the susceptibility profile. The obtained profiles are also perturbed due to the relatively large inhomogeneities in the template. The initial maximum of the profile at about 12 nm becomes less and less pronounced and after 29 Å thick iron layer, the profile doesn't reflect anymore the shape of the nanospheres. In certain regions on the substrate without spheres, the iron was deposited directly on the substrate which is reflected in the increase of the profile in the region between 0 nm to 7 nm. Some portion of the iron was deposited on the side of the spheres increasing the susceptibility in the region between 12 nm to 25 nm. The definite maximum above 25 nm corresponds to the iron on top of the spheres. In the case of

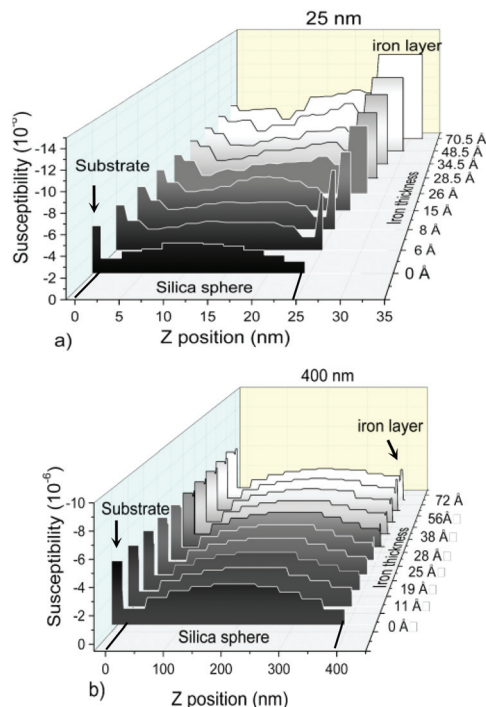


Fig. 4 The variation of the susceptibility as a function of the position along the z axis of the substrate for the 25 nm diameter (a) and 400 nm diameter (b) silica spheres. The zero distance represents the substrate/sphere interface.

400 nm diameter spheres, the evaporated iron thicknesses are almost negligible compared to the size of the spheres and therefore the susceptibility profiles remained mainly unchanged except for a small region at the top and the bottom of the spheres.

Based on the extracted layer profiles, the *in situ* recorded GISAXS images for both sphere sizes were calculated. Fig. 5 shows the recorded images for the 25 nm (top) and 400 nm diameter spheres (bottom) before and after ~ 70 Å iron deposition and the corresponding simulations. Left to the GISAXS images, a scheme of the simulated spheres with the assumed iron morphology is shown. In our model the coherent scattering is assumed and treated *via* a 2D paracrystal interference function based on a hexagonal lattice structure with a Cauchy distribution function. The system consisting of 400 nm diameter spheres could be well described by using a full sphere form factor and with the particle morphology of randomly oriented domains with an average size of 5 μm . In the case of 25 nm diameter particles, the characterization of the system was different because, in contrast to the 400 nm spheres, the particles could not be properly modeled by a perfect full sphere form factor. The small plateau in the susceptibility profile together with the FESEM image indicate that the shape of the small particles may deviate from the perfect sphere, therefore instead of using a full sphere form factor, it leads to a better result if we used a modified form factor, as presented in Fig. 5. In the simulation we assumed randomly oriented

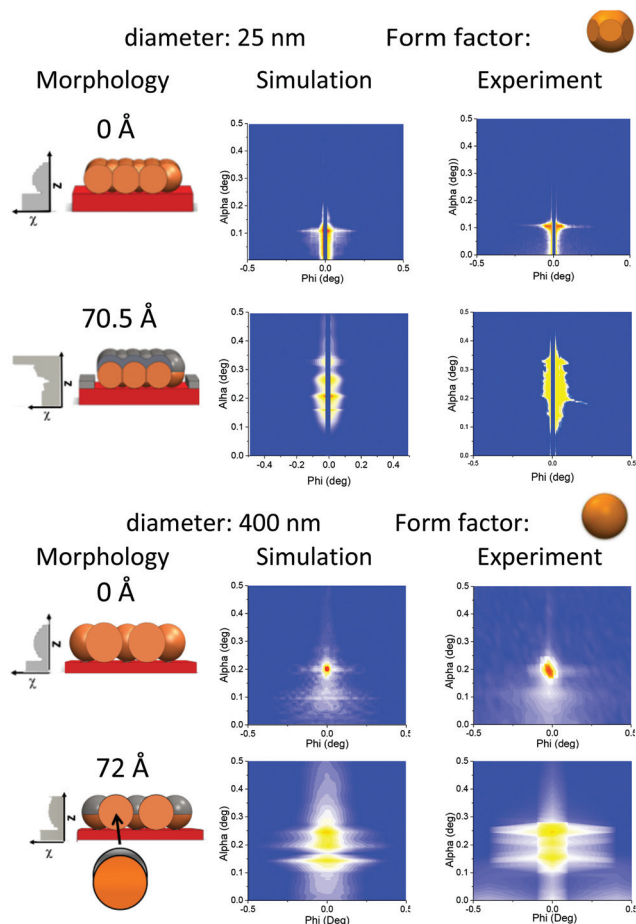


Fig. 5 GISAXS images recorded on 25 nm and 400 nm diameter spheres before and after iron deposition and the corresponding simulations. The simulated particle morphology with the corresponding susceptibility profile and the related form factor is given.

particle domains with an average size of 200 nm. Relying on the layer profiles extracted from XRR and on the simulated GISAXS images, it was found that in the case of the 25 nm diameter spheres, the evaporated iron forms a continuous layer on the top of the spheres (Fig. 5, top), hence the iron cannot be treated as a sum of individual caps formed on the spheres. Due to the larger interparticle distance and the lower ratio of the evaporated iron compared to the sphere size, the 400 nm diameter particles were modeled as independent particles with a small iron cap on top (Fig. 5, bottom). The cap has a thickness gradient, starting from the evaporated iron thickness at the top which decreases continuously as it goes down on the side of the spheres.

In order to follow the evolution of magnetism as well as to extract the depth dependence of magnetic moment configuration in iron grown on nanospheres, *in situ* nuclear forward scattering (NFS) measurements were performed (Fig. 6b–d). The depth dependence was obtained by measuring NFS spectra at different, carefully selected incident angles of the incoming beam: at 0.11° below the critical angle of silicon (0.12°), at 0.21° below the critical angle of iron (0.22°) and at 0.31° above both critical angles. The latter incident angles together with the corresponding critical angles are indicated in Fig. 6a.

The evaluation of the NFS data was based on the susceptibility profile obtained from X-ray reflectivity measurements. Utilizing the same sublayer structure, the hyperfine parameters were assigned to each of the sublayers but the complexity of the evaluation – due to the great amount of independent hyperfine parameters – made it necessary to make constraints between the parameters. The hyperfine parameters in the adjacent sublayers were correlated in such way that the very top of the sphere was described with one set of parameters and the

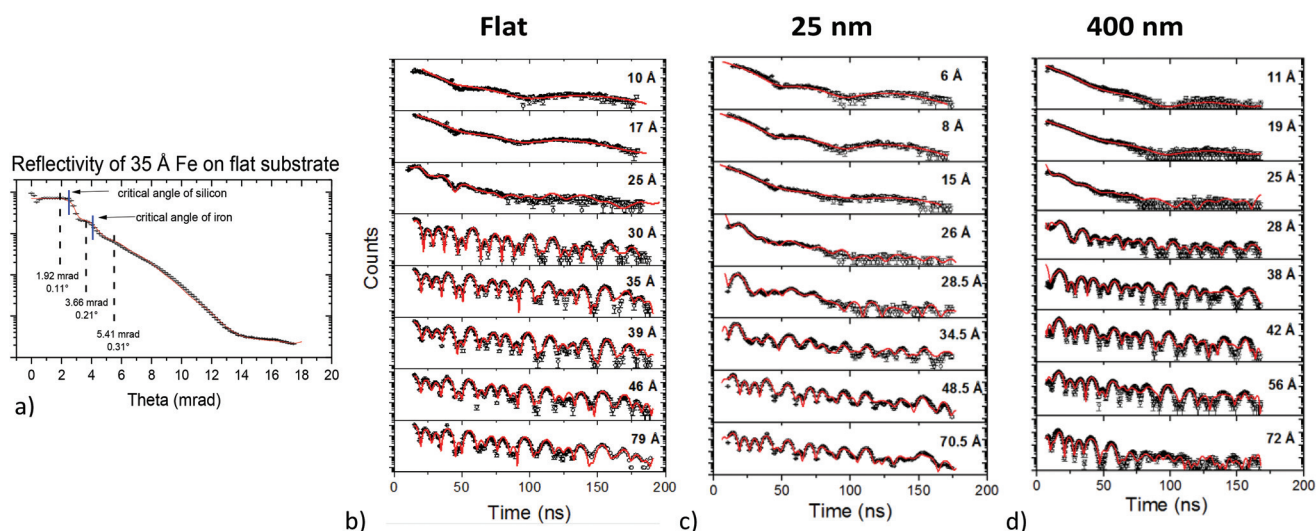


Fig. 6 (a) X-ray reflectivity curves measured on 35 Å iron on a flat substrate. Dashed lines represent the angles where time spectra were recorded and blue lines indicate the critical angle of silicon and iron. The red line corresponds to the simulated time resolved NFS spectra (black circles) measured at an incident angle of 0.11° after each iron deposition phase (b) on a flat Si substrate (c) on 25 nm and (d) on 400 nm diameter spheres.

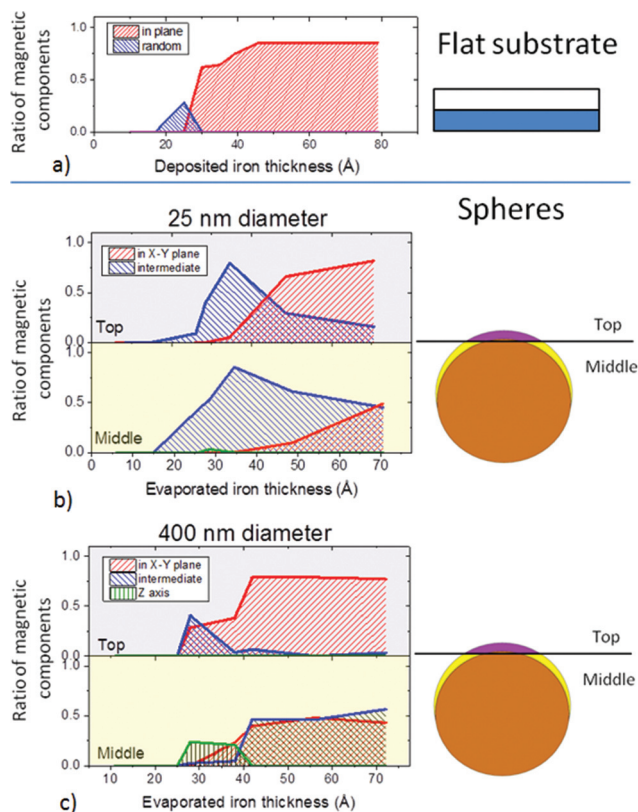


Fig. 7 Evolution of the magnetic component orientation with increasing iron thickness of (a) flat substrate, (b) 25 nm and (c) 400 nm diameter silica spheres. The green line corresponds to the magnetic orientation parallel to the z direction, the red line corresponds to the magnetization lying in the x–y plane and the blue line corresponds to the intermediate magnetization direction. For the 25 nm and 400 nm particles the frame is divided into two parts representing the ratio of the magnetic components on the top of the sphere and on the middle of the sphere as is indicated in the picture next to the frame.

middle of the sphere with another set of parameters as it is indicated in Fig. 7b and c. The NFS data obtained at different incident angles, corresponding to the same iron thickness, were fitted simultaneously.

At the lowest iron thicknesses (below ~ 20 Å) the NFS spectra do not depend on the substrate morphology. The iron layer was found to be non-magnetic and the time spectra could be fitted by a quadrupole splitting of $0.63(2)$ mm s^{-1} representing the symmetry breaking at the surface.

In the case of the flat Si sample, the first magnetic component appears at an iron thickness of 25 Å and gives a 28% contribution to the spectrum. Here the magnetic moments are oriented with an angle of 42° relative to the surface (Fig. 7a). With further iron deposition – as expected – the magnetization turned in plane due to the shape anisotropy.

The magnetization orientation varied in a more complex way when the iron deposition occurred on the nanosphere template. In Fig. 7, the contribution of the different magnetic components to the NFS spectrum is shown as a function of the deposited iron thickness. The components are grouped accord-

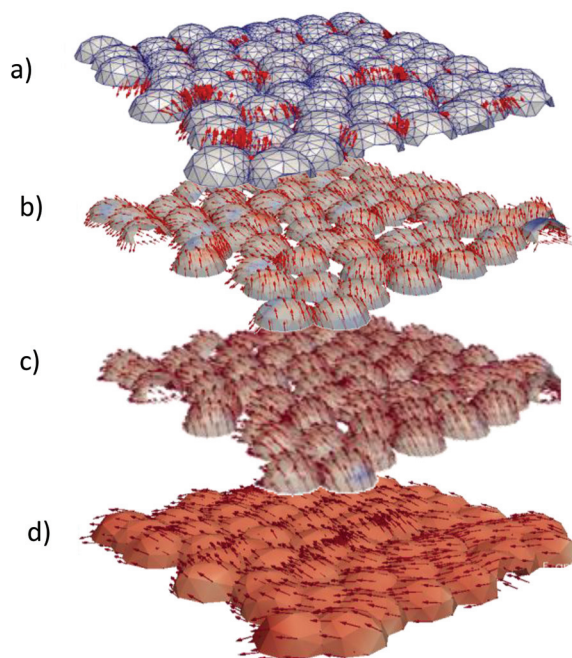


Fig. 8 Magnetic moment configuration calculated by micromagnetic simulation for (a) 26 Å, (b) 34.5 Å, (c) 48.5 Å and (d) 70.5 Å evaporated iron thickness on 25 nm diameter spheres. The blue color represents the magnitude of the z component while the red stands for the x–y in-plane component.

ing to their orientation: (a) lays in the x–y plane, (b) intermediate, meaning that it has an out of (x–y) plane angle distribution and (c) where it points along the z direction. In Fig. 7b and c, the frame is divided into two parts representing the top and the middle region of the spheres.

In the case of 25 nm diameter spheres, the first magnetic component in the spectrum appears as fast oscillations at the iron thickness of 26 Å. The analysis showed that the contribution of the magnetic component in the middle of the sphere is 44% while in the upper part it is only 9% and both have random angular distribution. A possible explanation is that, first, the regions where the spheres are in contact with each other become magnetic due to the locally increased iron concentration.

Micromagnetic simulations were performed in order to reconstruct the possible magnetic moment configuration. The 3D structure of the nanosphere template was constructed based on a representative FESEM image by taking the position and size of a set of 60 particles and in the simulation this 3D structure was periodically repeated. The saturation magnetization (M_s) was set to 1.7×10^6 A m^{-1} , the exchange stiffness constant to 1×10^{-11} A m^{-1} and no anisotropy was applied. According to the simulations shown in Fig. 8a the magnetic domains are spatially isolated from each other and distribute uniformly which makes this system interesting for magnetic applications. These magnetic volumes are expected to have magnetostatic interactions. By reaching an iron thickness of

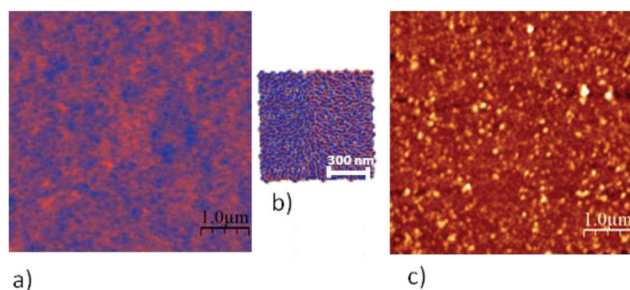


Fig. 9 (a) MFM image taken on 25 nm diameter nanospheres covered with ~ 70 Å iron and a 50 Å Nb capping layer. The magnetic tip was magnetized along the tip axis; hence the measurement was sensitive to the perpendicular component of the magnetization. (b) The simulated magnetic orientation distribution in the Fe layer and (c) the acquired topography image are shown.

~ 35 Å, the iron cap becomes essentially magnetic with intermediate magnetic distribution, but on the top a small fraction (5%) of the magnetic moments starts to turn in plane (Fig. 8b). It can be seen that the magnetic structure of the iron caps is not limited to only one particle but it involves several particles through exchange coupling. At an iron thickness of ~ 48 Å the magnetization on the top part mainly lays in plane. However, in the middle region, the vertical orientation is still distributed, but already, a rotation towards the x - y plane can be observed (Fig. 8c). By the last evaporation step the iron forms a continuous layer on the top of the spheres which was already seen from the reflectivity measurements (Fig. 8d). This might explain why it is favorable for the system magnetization to lay in the x - y plane with an off-plane distribution along the lower edge of the cap.

Fig. 9a shows the perpendicular magnetization component recorded on the 70.5 Å thick iron layer (covered by 50 Å Nb capping layer) and the simultaneously acquired AFM image (Fig. 9a and c). For comparison the result of micromagnetic simulation is plotted in the middle (Fig. 9b). The different colors represent the variation of the phase shift of the oscillation of the magnetic tip. The MFM measurement indicates that the sizes of magnetic domains are in the order of one micron, much larger than the size of the spheres and no correlation between the magnetic domains and the topography of the surface could be observed.

The evolution of the magnetism in the iron film deposited on the 400 nm diameter sphere template is shown in Fig. 7c. At 25 Å thick iron layer, the evaluation of the time spectra revealed that in the lower part of the cap, the magnetic moments point along the z direction and have $\sim 25\%$ magnetic fraction while on the top, the orientation is intermediate or lies in the x - y plane with about 50% contribution to the whole spectrum. It is known that an ultrathin iron film can exhibit complex magnetic structures up to several monolayers.^{50–52} Internal stress or asymmetric crystal lattice can also be the source of magnetic anisotropy.³⁰ In our case the orientation of magnetic moments along the z axis stems from the non-magnetic/magnetic transition region with an ultrathin iron

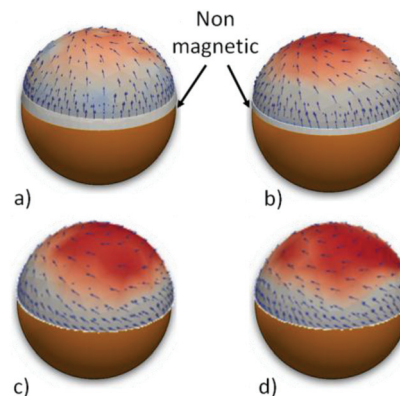


Fig. 10 The magnetic moment configuration calculated by micromagnetic simulation for (a) 28 Å, (b) 38 Å, (c) 42 Å and (d) 72 Å iron thicknesses on 400 nm diameter spheres. The blue color represents the magnitude of the z component while the red stands for the x - y in-plane component. The non-magnetic part of the iron layer is shown in gray.

film with gradient thickness on the side of the spheres. Also this gradient thickness is reflected in the reduction of ferromagnetism in the lower region which explains the different amounts of magnetic contribution in the top and lower part of the iron cap.

The micromagnetic model as well as the boundary conditions were tailored so that the resulting magnetic moment configuration would show agreement with the experimental data obtained from our nuclear resonant scattering experiments. A strict condition was that at the onset of magnetism, the magnetic moments should be aligned parallel to the z axis at the side of the sphere.

The micromagnetic model is shown in Fig. 10a. The simulation parameters were identical to what we applied for the 25 nm diameter spheres but in addition a small uniaxial anisotropy (K_u) along the z direction was assigned to the transition region in order to reproduce the magnetic configuration extracted from the NFS spectra. We have varied K_u between 0 and 5×10^5 J m⁻³ and the best fit to the experimental data was found at $K_u = 8 \times 10^4$ J m⁻³. According to the simulation the orientation of the magnetic moments turns from the z direction to the x - y plane and on the top it forms a vortex. With further iron deposition (at a thickness of 38 Å) the transition zone moves down on the side of the sphere reducing the effect of anisotropy. As a consequence the vortex starts to spread down on the iron cap resulting in an almost fully in-plane magnetization at the top region. In addition, at the lower region, a mixture of intermediate, plane parallel and plane perpendicular magnetic orientation could be observed (Fig. 10b). By reaching the 42 Å iron thickness the contribution of magnetic components becomes dominant in the spectrum. The vortex formation continues and the magnetic moments parallel to the z axis disappear even at the lower part of the cap. The simulated arrangement of the magnetic moments is shown in Fig. 10c. We found the best agreement with the extracted data applying a reduced uniaxial anisotropy of $K_u = 1.6 \times 10^4$ J m⁻³.

The further increase of the amount of deposited iron to 72 Å only results in a slight change in the magnetic structure (Fig. 10d).

The reason of this saturated behavior is different for the upper part and for the lower part of the iron cap. On the top of the spheres the vortex has formed already at the thickness of 42 Å and it doesn't change (significantly) with further iron evaporation explaining the saturated magnetic behavior in the upper part. On the other hand, this argument is not valid at the side of the sphere where one would expect the enhancement of the in-plane magnetization at the expense of the intermediate magnetic component. The magnetic saturation effect is caused by the presence of the nonmagnetic/magnetic interface together with an ultrathin iron film with gradient thickness on the side of the spheres. In our model the transition region with gradient iron thickness favors a magnetization orientation parallel to the z axis. With increasing thickness of evaporated iron, the transition zone moves down on the side of the sphere while its relative contribution decreases. This movement is faster at the beginning when the nonmagnetic/magnetic interface is positioned higher on the side and slows down as the transition zone approaches the lower side of the sphere and disappears when the iron thickness reaches the critical thickness everywhere. In the questioned thickness range (42 Å–72 Å) the transition zone already reached the bottom of the iron cap and cannot go further down. This is a steady state of the system until the thickness of the iron exceeds a critical iron thickness eliminating this transition zone.

In Fig. 11 the MFM and AFM images of the 72 Å thick iron (covered by 50 Å Nb capping layer) are shown. The MFM measurement features the perpendicular component of magnetization. The hexagonal structure built from the simulated iron caps is shown in Fig. 11b in order to compare the simulation with the measurement. Each iron cap, in contrast to the 25 nm spheres, has an individual magnetic structure. The micromagnetic simulation can be well correlated with the measurement, assigning the red regions to the magnetic vortices on the top with in-plane magnetization and the blue

regions to the intermediate component at the side of the sphere.

The two main differences between the 25 nm and 400 nm diameter spheres are: (i) the ratio of the evaporated material thickness compared to the particle diameter and (ii) the amount of contact area between the particles which is manifested in different interparticle interactions. In the case of the 25 nm spheres the spheres are in direct contact with each other and also deformed (according to GISAXS) implying a strong interparticle interaction. On the other hand, at low iron thicknesses the magnetic regions appear in the junction of the spheres creating a spatially isolated series of magnetic volumes. Since the magnetic stray fields are long ranged, these regions are expected to exhibit magnetostatic coupling. With further iron evaporation, the independent magnetic regions get in contact, introducing magnetic exchange interactions between the particles. When a continuous iron layer forms on the template, the exchange coupling becomes dominant and it is more reasonable to consider the system as a magnetic layer with local inhomogeneities than as a strongly coupled assembly of individual magnetic particles. In the case of 400 nm diameter particles, the spheres are not in direct contact and it has been shown for a short period planar nanodisk array that the interdot interaction has a strong destabilizing effect on the vortex spin state if the interdot distance is less than the radius of the nanodisk.⁵³ However, the destabilizing energy barrier is significantly reduced if a thickness gradient is introduced at the edge of the disks.⁵⁴ In our case the thickness gradient is given by the spherical template and for this reason a reduced or no magnetostatic coupling is expected.

4. Conclusions

In this paper we have investigated in detail how the size of silica nanospheres composing the template layer affects the evolution of magnetism in an iron ultrathin film, evaporated on top of the particles. We have focused on the thickness range of the nonmagnetic/magnetic transition. In order to gather extensive knowledge about the delicate interaction of the various parameters, we have carefully characterized the systems using different *in situ* (NFS, GISAXS, XRR) and *ex situ* (AFM, MFM, FESEM) techniques and with micromagnetic simulations we reconstructed the development of magnetic moment configurations.

We have found that the template morphology is cardinal and precise control of magnetization, necessary for industrial application, is not possible without careful selection of the size and distribution of the spherical particles. The ratio of the evaporated iron layer to the sphere size as well as the interparticle distances determine how the magnetic structure forms in the capping layer through the exchange coupling between particles and the shape of the particle.

When iron was evaporated on 25 nm diameter particles the iron starts to become magnetic in regions where the particles touch each other, creating a magnetic structure, consisting of

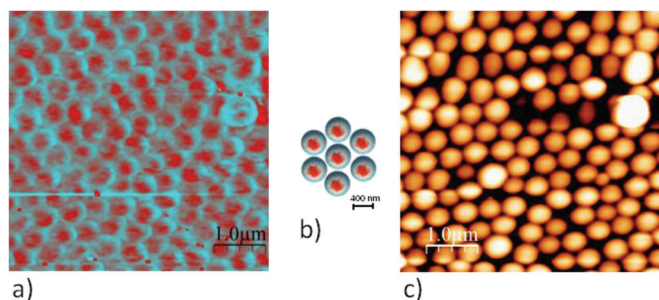


Fig. 11 (a) MFM images taken on an ~ 70 Å thick iron layer evaporated on 400 nm spheres. The magnetic tip was magnetized along the tip axis, implying that the measurement is sensitive to the perpendicular component of the magnetization. (b) The simulated hexagonal structure and (c) the AFM topography image.

isolated magnetic domains distributed uniformly which are essential for magnetic storage media. With further iron deposition a magnetic structure involving several particles could be observed due to the enhanced exchange interaction between the particles.

In the 400 nm diameter sphere particles, the system could be considered as a sum of individual magnetic particles. The formed magnetic structure clearly matches the topology of the spheres. Vortex formation on the top of the cap and magnetic anisotropy along the *z* axis at the nonmagnetic/magnetic interface were found. With increasing iron thickness, the vortex spreads down the sphere thus eliminating the *z* component of magnetization at the lower edge of the caps.

Thus, our study shows that the magnetic structure can be tailored not only by varying the morphology of the template but also by tuning the thickness of the magnetic layer. In this respect our study may devise routes in line with the requirements for 20 Tbit per inch² magnetic storage capacity.

Acknowledgements

The authors would like to thank Eszter Gergely-Fülöp for preparation of the Langmuir–Blodgett layers, Szilárd Sajti and László Deák for their valuable support in data evaluation and Jean-Philippe Celse for technical support. The European Synchrotron Radiation Facility is acknowledged for beamtime provision at ID18. Support from the Hungarian Research grants OTKA PD 105173, and OTKA K 112114 is highly appreciated. A. D. is supported by the János Bolyai Research grant of the Hungarian Academy of Sciences.

Notes and references

- G. Binasch, P. Grünberg, F. Saurenbach and W. Zinn, *Phys. Rev. B: Condens. Matter*, 1989, **39**, 4828.
- M. N. Baibich, J. M. Broto, A. Fert, F. N. van Dau, F. Petroff, P. Eitenne, G. Creuzet, A. Friederich and J. Chazelas, *Phys. Rev. Lett.*, 1988, **61**, 2472.
- M. Julliere, *Phys. Lett.*, 1975, **54A**, 225–226.
- J. Mathon and A. Umerski, *Phys. Rev. B: Condens. Matter*, 2001, **63**, 220403.
- U. Boettcher, H. Li and F. E. Talke, *IEEE Trans. Magn.*, 2011, **47**, 1823.
- D. G. Merkel, L. Bottyán, F. Tanczikó, Z. Zolnai, N. Nagy, G. Vértesy, J. Waizinger and L. Bommer, *J. Appl. Phys.*, 2011, **109**, 124302.
- M. Futamoto, Y. Hirayama, Y. Honda and A. Kikukawa, *NATO Sci. Ser.*, 2001, **41**, 103.
- M. Albrecht, C. T. Rettner, A. Moser, M. E. Best and B. D. Terris, *Appl. Phys. Lett.*, 2002, **81**, 2875.
- N. Honda, S. Takahashia and K. Ouchi, *J. Magn. Magn. Mater.*, 2008, **320**, 2195.
- K. Matsumoto, A. Inomata and S.-Y. Hasegawa, *Fujitsu Sci. Tech. J.*, 2006, **42**, 1.
- J. Choi, N. C. Park, K. S. Park and Y. P. Park, *Jpn. J. Appl. Phys.*, 2013, **52**, 09LF02.
- M. Todorovic, S. Shultz, J. Wong and A. Scherer, *Appl. Phys. Lett.*, 1999, **74**, 2516.
- J.-W. Liao, U. Atxitia, R. F. L. Evans, R. W. Chantrell and C.-H. Laim, *Phys. Rev. B: Condens. Matter*, 2014, **90**, 174415.
- H. J. Richter, A. Lyberatos, U. Nowak, R. F. L. Evans and R. W. Chantrell, *J. Appl. Phys.*, 2012, **111**, 033909.
- I. Gurrappa and L. Binder, *Sci. Technol. Adv. Mater.*, 2008, **9**, 043001.
- Z. Huang, N. Geyer, P. Werner, J. de Boor and U. Gösele, *Adv. Mater.*, 2011, **23**, 285.
- A. R. Rakkesh and S. Balakumar, *J. Nanosci. Nanotechnol.*, 2015, **15**, 4316.
- O. Bauder, A. Seiler, S. Ibrahimkuty, D. G. Merkel, B. Krause, R. Rüffer, T. Baumbach and S. Stankov, *J. Cryst. Growth*, 2014, **400**, 61.
- N. Nagy, A. E. Pap, A. Deák, E. Horváth, J. Volk, Z. Hórvölgyi and I. Bársony, *Appl. Phys. Lett.*, 2006, **89**, 063104.
- N. Nagy, Z. Zolnai, E. Fülöp, A. Deák and I. Bársony, *Appl. Surf. Sci.*, 2012, **259**, 331.
- Z. Zolnai, *Appl. Surf. Sci.*, 2013, **281**, 17.
- D. P. Tran, T. J. Macdonald, B. Wolfrum, R. Stockmann, T. Nann, A. Offenhausser and B. Thierry, *Appl. Phys. Lett.*, 2014, **105**, 231116.
- K. Ueno, S. Juodkazis, V. Mizeikis, K. Sasaki and H. Misawa, *J. Am. Chem. Soc.*, 2006, **128**, 14226.
- J. Fu, J. Zhang, Y. Peng, J. Zhao, G. Tan, N. J. Mellors, E. Xie and W. Han, *Nanoscale*, 2012, **4**, 3932.
- S. Yang and Y. Lei, *Nanoscale*, 2011, **3**, 2768.
- G. L. Nealon, B. Donnio, R. Greget, J. Kappler, E. Terazzib and J.-L. Gallani, *Nanoscale*, 2012, **4**, 5244.
- K. B. Blodgett and I. Langmuir, *Phys. Rev.*, 1937, **51**, 964.
- M. E. Diaz and R. L. Cerro, *Physicochemistry and Hydrodynamics of Langmuir-Blodgett Depositions*, VDM Verlag, Saarbrücken, Germany, 2008.
- T. C. Ulbrich, D. Makarov, G. Hu, I. L. Guhr, D. Suess, T. Schrefl and M. Albrecht, *Phys. Rev. Lett.*, 2006, **96**, 077202.
- M. Albrecht, G. Hu, I. L. Guhr, T. C. Ulbrich, J. Boneberg, P. Leiderer and G. Schatz, *Nat. Mater.*, 2005, **4**, 203.
- R. Streubel, D. Makarov, F. Kronast, V. Kravchuk, M. Albrecht and O. G. Schmidt, *Phys. Rev. B: Condens. Matter*, 2012, **85**, 174429.
- R. Streubel, D. J. Thurmer, D. Makarov, F. Kronast, T. Kosub, V. Kravchuk, D. D. Sheka, Y. Gaididei, R. Schäfer and O. G. Schmidt, *Nano Lett.*, 2012, **12**, 3961.
- J. Wang and J. Zhang, *Int. J. Solids Struct.*, 2013, **50**, 3597.
- K. Schlage, S. Couet, S. V. Roth, U. Vainio, R. Rüffer, M. M. Abul Kashem, P. Müller-Buschbaum and R. Röhlberger, *New J. Phys.*, 2012, **14**, 043007.
- W. Stöber, A. Fink and E. J. Bohn, *J. Colloid Interface Sci.*, 1968, **26**, 62.
- Z. Zolnai, N. Nagy, A. Deák, G. Battistig and E. Kótai, *Phys. Rev. B: Condens. Matter*, 2011, **83**, 233302.

- 37 Z. Zolnai, A. Deák, N. Nagy, A. L. Tóth, E. Kótai and G. Battistig, *Nucl. Instrum. Methods Phys. Res., Sect. B*, 2010, **262**, 79.
- 38 S. Stankov, R. Rüffer, M. Sladeczek, M. Rennhofer, B. Sepiol, G. Vogl, N. Spiridis, T. Ślęzak and J. Korecki, *Rev. Sci. Instrum.*, 2008, **79**, 045108.
- 39 R. Rüffer and A. I. Chumakov, *Hyp. Int.*, 1996, **97**, 589.
- 40 See details at: <http://www.esrf.eu/files/live/sites/www/files/Instrumentation/DetectorsAndElectronics/maxipix/Maxipix-Technical.pdf>.
- 41 See <http://gwyddion.net> for more details about the program.
- 42 I. Horcas, R. Fernández, J. M. Gómez-Rodríguez, J. Colchero, J. Gómez-Herrero and A. M. Baro, *Rev. Sci. Instrum.*, 2007, **78**, 013705.
- 43 T. Fischbacher, M. Franchin, G. Bordignon and H. Fangohr, *IEEE Trans. Magn.*, 2007, **43**, 2896.
- 44 T. L. Gilbert, *Phys. Rev.*, 1955, **100**, 1243.
- 45 U. Ayachit, *The ParaView Guide: A Parallel Visualization Application*, Kitware, 2015, ISBN 978-1930934306.
- 46 S. Sajti, L. Deák and L. Bottyán, 2009, arXiv:0907.2805, <http://www.fs.kfki.hu>.
- 47 L. Deák, L. Bottyán, D. L. Nagy and H. Spiering, *Physica B*, 2001, **297**, 113.
- 48 C. Durniak, M. Ganeva, G. Pospelov, W. Van Herck and J. Wuttke, BornAgain - Software for simulating and fitting X-ray and neutron small-angle scattering at grazing incidence, 2015, <http://www.bornagainproject.org>.
- 49 L. Deák, L. Bottán, D. L. Nagy and H. Spiering, *Phys. Rev. B: Condens. Matter*, 1996, **53**, 6158.
- 50 M. Ślęzak, T. Ślęzak, K. Freindl, W. Karás, N. Spiridis, M. Zając, A. I. Chumakov, S. Stankov, R. Rüffer and J. Korecki, *Phys. Rev. B: Condens. Matter*, 2013, **87**, 134411.
- 51 M. D. Martins and W. A. A. Macedo, *Phys. Status Solidi A*, 2002, **189**, 269.
- 52 A. Hahlin, "Magnetism and Structure of Thin 3D Transition Metal Films" Digital Comprehensive Summaries of Uppsala Dissertations from the Faculty of Science and Technology, 2003.
- 53 K. Y. Guslienko, V. Novosad, Y. Otani, H. Shima and K. Fukamichi, *Phys. Rev. B: Condens. Matter*, 2001, **65**, 024414.
- 54 N. Martin, N.-C. Bigall, I. Monch, T. Gemming, A. Eychmüller, R. Mattheis, R. Schafer, L. Schultz and J. McCord, *Adv. Funct. Mater.*, 2011, **21**, 891.